Received: 17 October 2018 | Revised: 6 December 2018 | Accepted: 20 December 2018

DOI: 10.1002/ese3.275

Energy Science & Engineering
Open Access

RESEARCH ARTICLE

Methane adsorption constrained by pore structure in high-rank coals using FESEM, CO_2 adsorption, and NMRC techniques

Tingting Yin[1,2] | **Dameng Liu**[1,2] | **Yidong Cai**[1,2] | **Yingfang Zhou**[3]

[1]School of Energy Resources, China University of Geosciences, Beijing, China

[2]Coal Reservoir Laboratory of Natural Engineering Research Center of CBM Development & Utilization, China University of Geosciences, Beijing, China

[3]School of Engineering, King's College, University of Aberdeen, Aberdeen, UK

Correspondence
Yidong Cai, School of Energy Resources, China University of Geosciences, Beijing, China
Email: yidong.cai@cugb.edu.cn

Abstract

To evaluate the impacts of nanopores of high-rank coals on coalbed methane adsorption and storage, 12 anthracite and semianthracite coal samples from Yangquan and Shouyang blocks in the Qinshui Basin were investigated. Field emission scanning electron microscopy (FESEM) and CO_2 adsorption combined with nuclear magnetic resonance cryoporometry (NMRC) experiments were used to evaluate the pore structure with diameters ranging from 0 to 500 nm and their impact on adsorption capacity based on qualitative and quantitative analysis. The results show that a coalification jump from semianthracite to anthracite occurred in the study area due to the magmatic intrusion. In the process, the volume of supermicropores and micropores largely increased while the volume of transition pores and mesopores decreased slightly. Additionally, vitrinite gets purified and enriched during the rapid maturation of coal reservoir, which is beneficial to the microporous structure development. The pore size distribution (PSD) of anthracite is mainly divided into two types, which are in serrated and decreasing forms, respectively. Higher vitrinite content can promote the formation of decreasing type (type II), which corresponds to a lower degree of complexity. The fractal dimensions indicate that the heterogeneity of coal samples is increasing with the decrease in pore size. Accordingly, the increase in pore heterogeneity corresponds to the lower adsorption capacity. The main pore sizes that contribute to CBM adsorption include two parts: 25-30 nm and 50-60 nm. For the supermicropores with large specific surface areas, the pore system detected by CO_2 molecules is not conducive to CBM adsorption, while the increase in pore volume can improve the adsorption rate and capacity of CO_2. These findings are vital for a precisely understanding of nanoscale pores as well as future CBM exploitation.

KEYWORDS

Coalbed methane, DFT theory, experiment method, fractal dimension, magmatic intrusion

1 | INTRODUCTION

Coalbed methane (CBM) has recently become a large focus of energy exploration as a significant supplement to clean energy resources.[1–3] The CBM reserves in China have reportedly reached 37 trillion m^3.[4] The production of CBM is a comprehensive process of gas desorption, diffusion, and Darcy flow. The basis of the success of CBM extraction lies in the adsorption and storage capacity of the pore system of coal.[5] Pore structure characterization of coals is mainly conducted

through two methods: (1) Imaging description due to well-developed nanoscale pores and their high heterogeneity, new techniques are continuously being applied in CBM reservoirs to improve resolution and accuracy, including two-dimensional imaging methods (such as field emission scanning electron microscopy (FESEM),[6] broad ion beam-scanning electron microscopy (BIB-SEM)[7], and confocal laser scanning microscopes(CLSM)[8]), as well as three-dimensional imaging methods (for example, focused ion beam-scanning electron microscopy (FIB-SEM),[9] focused ion beam-Helium ion microscopy (FIB-HIM),[10] atomic force microscopy (AFM)[11], and nanocomputed topography (CT)[12]). The ranges of pore size in coals observed by different methods are variable because of the differences in experimental principles. For

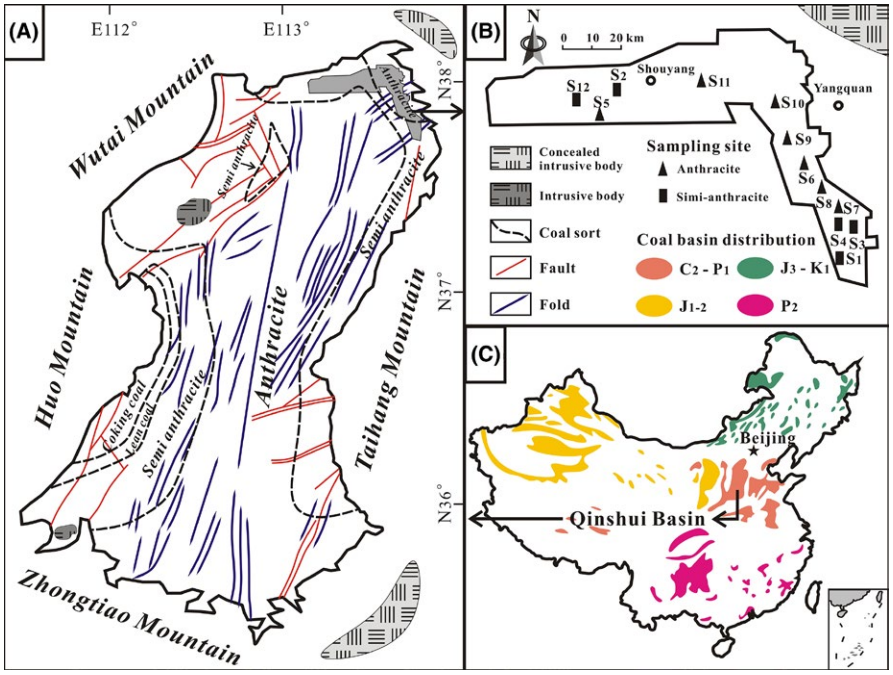

FIGURE 1 Regional geological map. A, Position and tectonic characteristics of the Qinshui Basin. B, the distribution of the sample points. C, Coal basin distribution in China

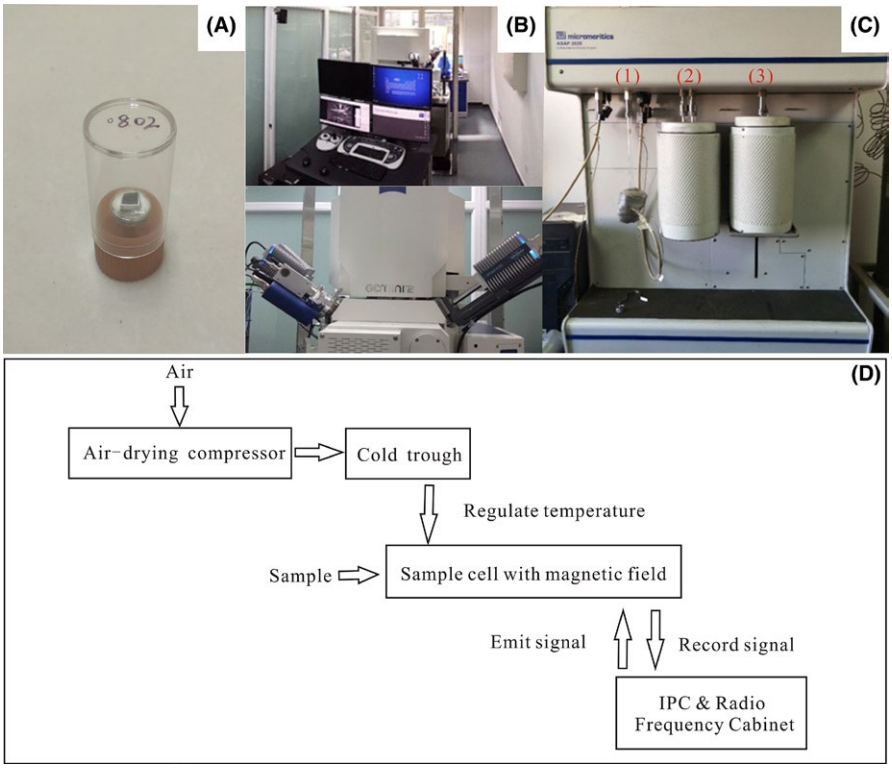

FIGURE 2 Device and sample diagrams. A, The polished sample for FESEM observation. B, FESEM device. C, CO_2 adsorption device (1) degassing plant (2) cooling trap (3) adsorption station). D, The flow chart of NMRC experiment

instance, FIB-HIM has the highest resolution and can detect pores with diameters as small as 5 nm. FESEM with a secondary electron (SE) detector can be used for direct imaging and local quantitative calculation for pores larger than 10 nm in size. Components including organic matter (OM) and minerals can be recognized by Gray Threshold.[13–15] Moreover, compared with other methods, FESEM have low requirements for working conditions with an acceleration voltage <2Kv.[16] (2) Fluid intrusion: three additional categories are used for the detection of pore size scope: (1) The first kind of methods mainly focuses on the adsorption pores with a small diameter. As the decisive role of nanoscale pores in the adsorption capacity, many new methods have been applied to coals, such as low-temperature nitrogen and carbon dioxide (CO_2) adsorption,[17,18] small angle X-ray scattering (SAXS),[19] small angle neutron scattering (SANS),[20] and nuclear magnetic resonance cryoporometry (NMRC).[21] A CO_2 adsorption test can detect the pore structures with diameter <1 nm due to the small diameter (0.33 nm), strong adsorption potential and activated diffusion of the CO_2 molecule,[17] which is not possible with other methods. Moreover, the specific surface area and pore volume from CO_2 adsorption is higher than those from low-temperature nitrogen adsorption.[18] The PSD measured by NMRC ranges from 1 to 500 nm, and the accuracy of the results is higher than that of low-temperature nitrogen adsorption, especially for micropores.[21,22] (2) The major research section is seepage pore and fracture, such as mercury intrusion porosimetry (MIP). Since the pores in CBM reservoirs have strong compressibility,[23] the results of adsorption pores obtained by this means are usually inaccurate. (3) Represented by nuclear magnetic resonance (NMR), this method is characterized by a wide measuring range from nano- to micron-scale pores. However, the PSD curves based on T_2 spectrum exhibit high smoothness and single peaks of adsorption pores, seepage pores, and fractures, separately, which shows the data with poor accuracy.[24–26]

Nanopores, including micropores (2-10 nm in diameter), transition pores (10-100 nm in diameter), and mesopores

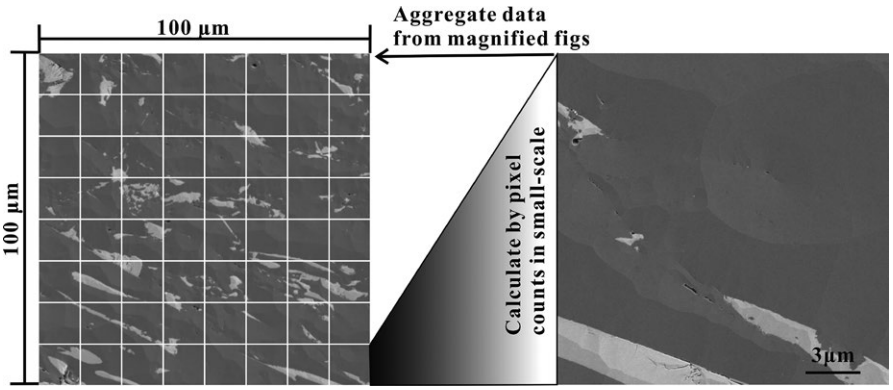

FIGURE 3 Quantitative processing for FESEM images by ATLAS software

TABLE 1 Pore volume and adsorption rate by CO_2 adsorption analyses in high- rank coals

Sample no.	$R_{o,m}$(%)	Coal rank	Pore volume (cm^3/g)		Adsorption rate ($cm^3/(g{\cdot}min)$)	
			D-A	DFT	Average	Maximum
S1	2.44	Semianthracite	0.06036	0.02372	0.01679	1.96944
S2	2.34	Semianthracite	0.05408	0.02276	0.014	1.80595
S3	2.32	Semianthracite	0.06086	0.02934	0.0146	2.06577
S4	2.36	Semianthracite	0.0617	0.02884	0.01516	2.29052
S5	3.35	Anthracite	0.09587	0.0367	0.04549	3.66489
S6	3.22	Anthracite	0.10247	0.04423	0.04172	4.21933
S7	3.25	Anthracite	0.10322	0.04402	0.04154	3.65513
S8	3.16	Anthracite	0.10252	0.04373	0.04551	4.18709
S9	3.00	Anthracite	0.09808	0.04038	0.03992	3.89528
S10	3.03	Anthracite	0.09924	0.04398	0.03962	3.64484
S11	3.09	Anthracite	0.10109	0.04392	0.04506	4.19696
S12	2.22	Semianthracite	0.08014	0.03075	0.02797	2.69192

$R_{o,m}$ represents maximum vitrinite reflectance under oil immersion(data from ref[22]); D-A and DFT means the data calculated based on Dubinin-Astakhov and Density Functional Theory model, respectively.

TABLE 2 Pore volume at different pore size based on NMRC measurements

Sample no.	Pore volume(cm^3/g)			
	V_1	V_2	V_3	V_T
S1	0.0009	0.0027	0.0037	0.0072
S2	0.0033	0.0038	0.0009	0.0080
S3	0.0069	0.0015	0.0012	0.0096
S4	0.0075	0.0063	0.0011	0.0149
S5	0.0058	0.0058	0.0006	0.0122
S6	0.0068	0.0090	0.0015	0.0173
S7	0.0101	0.0040	0.0017	0.0159
S8	0.0086	0.0047	0.0007	0.0139
S9	0.0107	0.0035	0.0011	0.0153
S10	0.0065	0.0048	0.0009	0.0122
S11	0.0066	0.0028	0.0009	0.0104
S12	0.0089	0.0157	0.0003	0.0250

V_1, V_2, V_3 and V_T respect the pore volume of micropores, transition pores, mesopores and total pores with diameter from 1 to 500 nm.

(100-1000 nm in diameter), with relatively small pore sizes and large specific surface areas are the main storage space of CBM. These occupy up to 90% of the total amount according to results.[19,27] The coal reservoir in the Qinshui Basin is characterized by high thermal evolution and nanopore proportions due to the presence of magmatic hydrothermal fluids.[28] Therefore, a systematic analysis focused on the nanoscale pore structure with a small diameter based on various improved methods is required. In this paper, 12 anthracite and semianthracite coal samples from the Qinshui Basin were collected to study the pore system of 0-500 nm diameter with both imaging description and fluid instruction methods using FESEM, CO_2 adsorption, and NMRC techniques: (1) the pore structure characteristics including pore size distribution, morphology, and fractal dimensions were systematically discussed; (2) the geological conditions were considered to analyze the coalification jump from semianthracite to anthracite; (3) the contribution of different pore size segments to CBM adsorption capacity was quantificationally summarized to provide an important basis

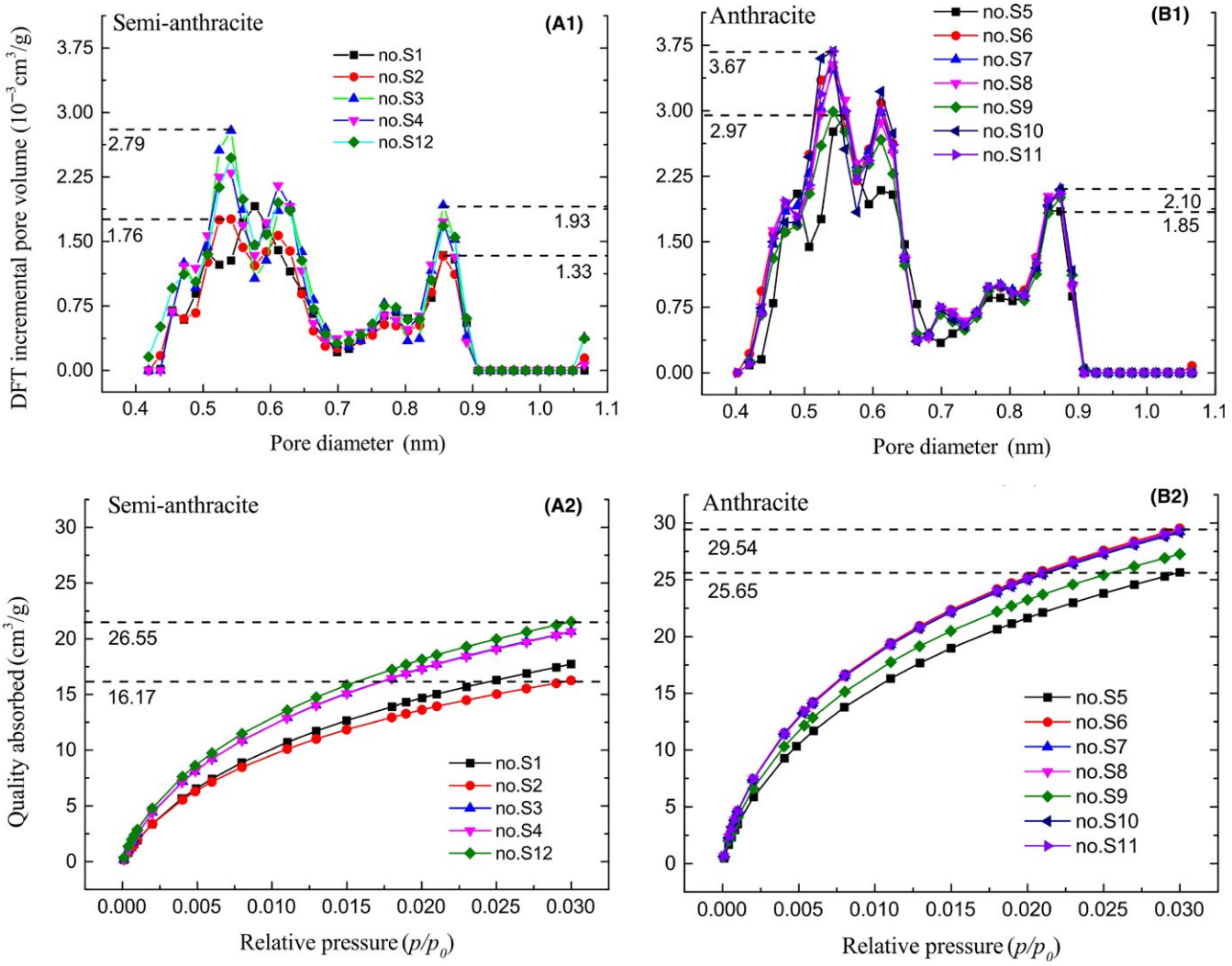

FIGURE 4 The CO_2 adsorption results for semianthracite and anthracite (A1,A2) PSD curves (B1,B2) Adsorption curves

for CBM prediction and adsorption capacity evaluation for high-rank coals in the Qinshui Basin.

2 | MATERIALS AND METHODS

2.1 | Sample preparation and petrological characteristics

Twelve semianthracite and anthracite coal samples were collected from Yangquan and Shouyang blocks in the Qinshui Basin (Figure 1). Standard coal analyses, including the maximum vitrinite reflectance ($R_{o,m}$), coal composition, and proximate analysis, were conducted at the Key Laboratory of Marine Reservoir Evolution, China University of Geosciences (Beijing) following the standards ISO 7404.3-1994, ISO 7404.5-1994 and ISO 17246-2010, respectively. Details of experimental equipment and procedures were reported in our previous research.[29] The results show that $R_{o,m}$ ranges from 2.22% to 3.35%, with organic matter content of 91.7%-97.5%, pyrite content of 0.1%-1.2%, and other mineral content of 2.3%-8.1%. The proximate analysis indicated that the moisture, ash, volatile material, and fixed carbon content, respectively, vary from 0.88 to 1.63%, 8.78 to 13.41%, 12.43 to 18.38%, and from 70.09 to 74.31%. (Data from ref [22])

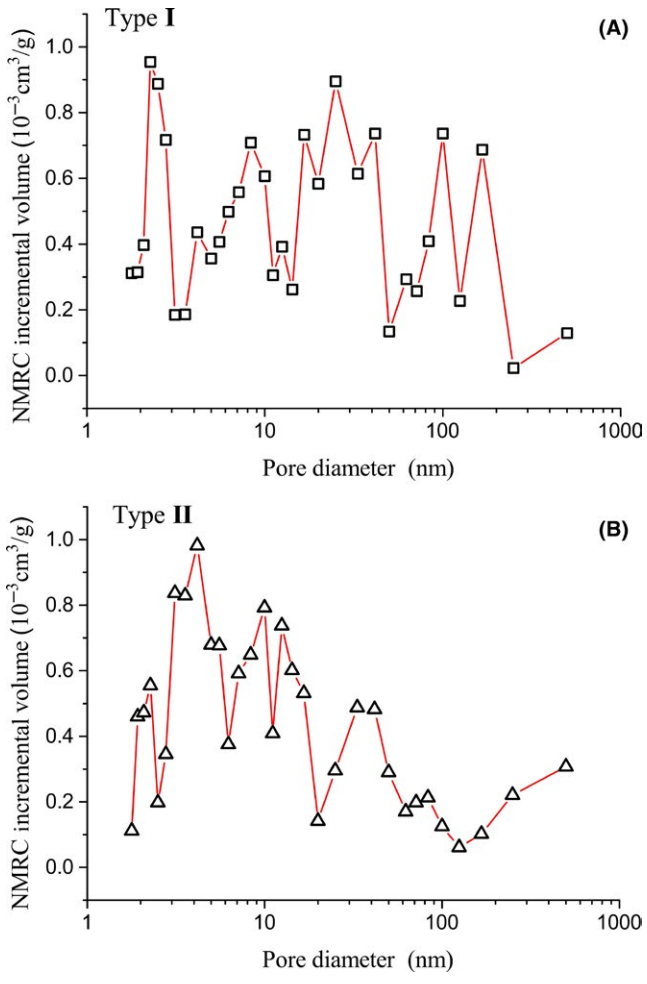

FIGURE 5 Two types of PSD curves from NMRC experiment. A, type I. B, type II

2.2 | Experiment and quantitative methods

2.2.1 | FESEM experiment

Prior to imaging, samples were first polished by argon ion under stress-free conditions on LEICA.EM.TIC.3X equipment to make a smooth and damage-free surface.[15] Second, the samples with a polished surface of 5 mm × 5 mm were immediately analyzed using FESEM to prevent air pollution (shown in Figure 2A). The imaging was performed on Merlin of ZEISS (shown in Figure 2B) with acceleration voltage of 1.2 kV. The pixel size was 5 nm, and the minimum pores that could be clearly observed are approximately 10 nm in diameter. In the SE mode, organic matter appears darker gray, minerals are lighter gray to white, and pores are black based on atomic number contrast.[30] Sometimes, the sharp and protruding morphology at the pore edges may induce charge accumulation of second electrons and produce a luminous edge in the periphery of black pores, causing an underestimate of pore proportion.

As shown in Figure 3, areas of 100 μm × 100 μm were randomly selected using ATLAS software, and the area was divided into small areas for amplification and observation. Under the condition of low magnification, the heterogeneity and PSD characteristics in small scale can be qualitatively analyzed. At larger magnification, the proportion and types of pore and components can be calculated based on pixel counts. The formulas are derived as follows[13]:

Areal porosity:

$$\phi = \sum_{1}^{n} \mathrm{SF_n} A_\phi / A_\mathrm{T}, \tag{1}$$

where n is the number of small regions after division; SF_n is the scaling factor corresponding to the nth area; A_ϕ is the area occupied by pores; A_T is the total area.

Proportion of OM-hosted pores to total pores:

$$\phi_\mathrm{OM} = \sum_{1}^{n} \mathrm{SF}_n A_{\phi\mathrm{OM}} / A_\phi, \tag{2}$$

where $\mathrm{A}_{\phi\mathrm{OM}}$ is the area of OM-hosted pores.

In a similar way, proportion of mineral-associated pores to total pores:

$$\phi_\mathrm{MIN} = \sum_{1}^{n} \mathrm{SF}_n A_{\phi\mathrm{MIN}} / A_\phi, \tag{3}$$

where $A_{\phi\mathrm{MIN}}$ is the area of mineral-associated pores.

Proportion of OM component:

$$P_\mathrm{OM} = \sum_{1}^{n} \mathrm{SF}_n A_\mathrm{OM} / \left(\mathrm{m}A_\mathrm{OM} + A_\mathrm{MIN}\right), \tag{4}$$

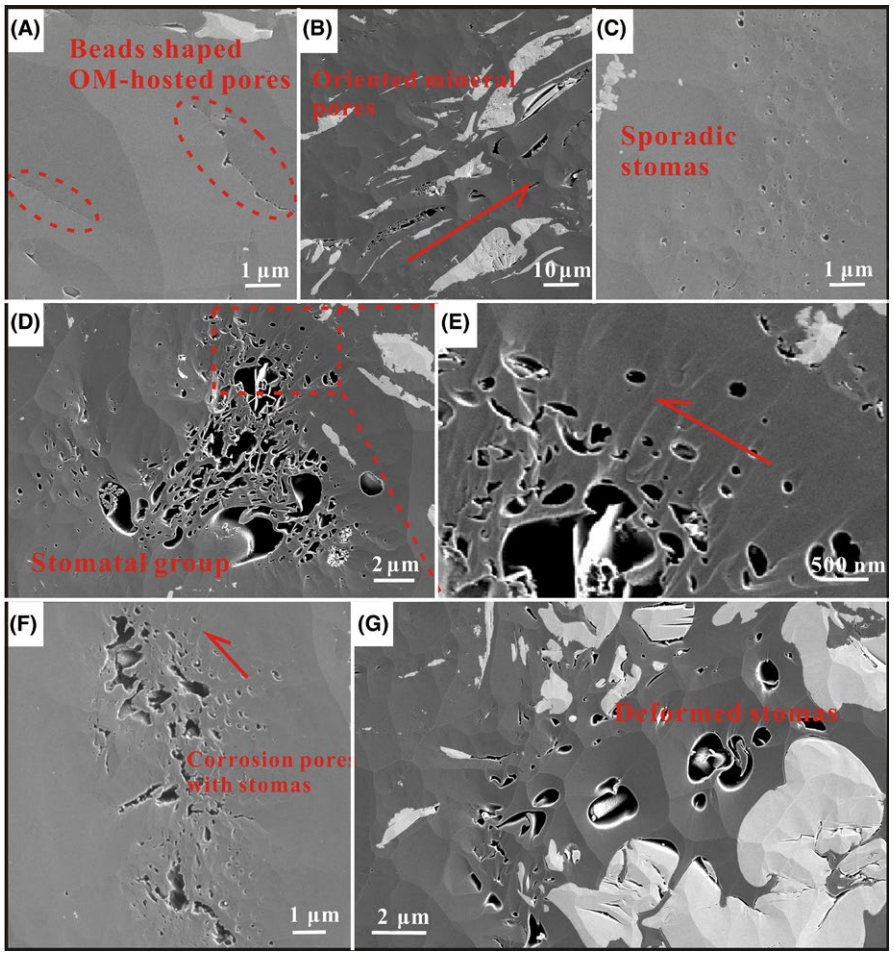

FIGURE 6 Images under FESEM

where A_{OM} and A_{MIN} are the area of OM and mineral component, respectively.

Similarly, the proportion of mineral component:

$$P_{MIN} = \sum_{1}^{n} SF_n A_{MIN} / \left(A_{OM} + A_{MIN}\right) \quad (5)$$

2.2.2 | CO_2 adsorption experiment

CO_2 adsorption measurements were conducted with a Micromeritics ASAP 2020 specific surface area and porosity analyzer (shown in Figure 2C). It comprised a degassing plant, a cooling trap, and an adsorption station. Powdery coal samples (60-80 meshes) were first put into the degassing plant. Meanwhile, CO_2 was imported into the cooling trap for cooling and purification. Subsequently, the samples were put into the adsorption station. By injecting CO_2 and equilibrating the sample, the coal particles can reach the equilibrium state under a saturation pressure. And the pore size distribution can be calculated according to the amount of gas adsorbed during pressurization.

The adsorption data were finally determined based on Dubinin-Radushkevich (D-R), Dubinin-Astakhov (D-A), and Density Functional Theory (DFT) models, respectively. D-R and D-A models are a kind of micropore gas filling theory based on the Polanyi potential energy principle.

D-R model: in a single adsorbate system, taking characteristic adsorption energy as E, the adsorbed volume by adsorbate is derived as follows[31]:

TABLE 3 Areal porosity and component proportion based on FESEM analyses

Areal porosity (%)					Component proportion (%)	
Total pores	$\phi_{>500nm}$	$\phi_{<500nm}$	ϕ_{OM}	ϕ_{MIN}	ϕ_{OM}	ϕ_{MIN}
0.44	0.06	0.38	0.11	0.33	91.91	8.09

$\phi_{>500nm}$, $\phi_{<500nm}$, ϕ_{OM} and ϕ_{MIN}, respect the proportion of pores with diameter >500 nm, <500nm, OM-hosted pores and mineral-associated pores, respectively. P_{OM} and P_{MIN} respect the proportion of OM and minerals, respectively.

$$\theta = \frac{V}{V_0} = \exp\left[-\left(\frac{RT}{\beta E_0}\ln\frac{p_0}{p}\right)^2\right], \quad (6)$$

where V is the adsorbed volume at relative pressure p_0/p; V_0 is the maximum volume of adsorbed gas; θ is the micropore filling rate; E_0 is the characteristic adsorption energy that can reference fluid; β is similarity factor; R is the gas constant; and T is the equilibrium temperature. Using logarithms for Equation 6, this can be revised as follows:

$$\ln V = \ln V_0 - \left(\frac{RT}{\beta E_0}\right)^2\left(\ln\frac{p_0}{p}\right)^2 \quad (7)$$

Therefore, through the linear fitting of InV and $\left(\ln\frac{p_0}{p}\right)^2$, total pore volume is attainable through intercept. Replacing the exponent 2 in Equations 6 and 7 with n, the D-A formula can be obtained.

The DFT model is a statistical mechanics method for describing the adsorbed substance at the molecular level. Based on the adsorption isotherms acquired by the microscopic method and experimental isotherms measured in porous media, the generalized adsorption isotherm (GAI) equation is defined as follows[32]:

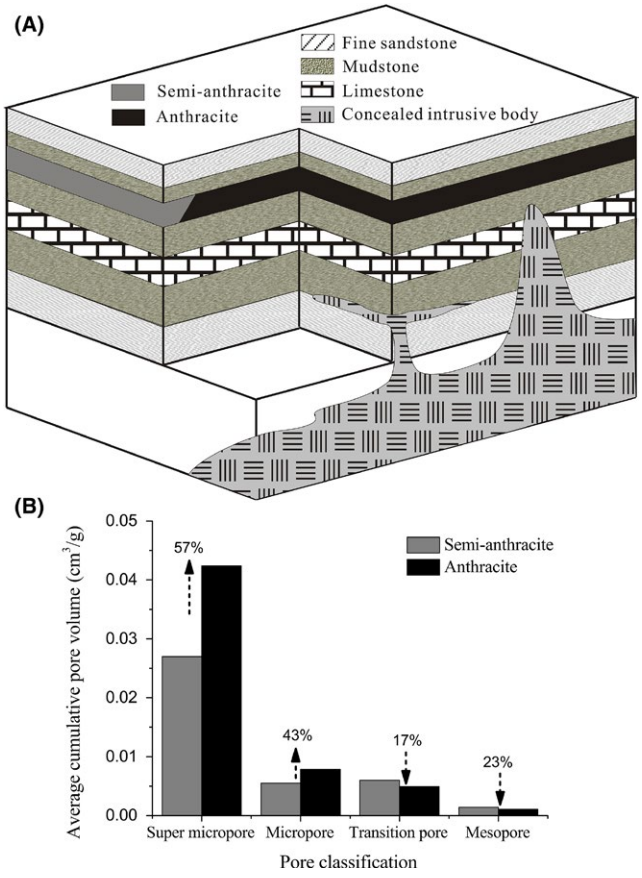

FIGURE 7 A, Magmatic intrusion pattern graph. B, The changes of the average cumulative pore volume from semianthracite to anthracite caused by the magmatic intrusion

$$N\left(\frac{P}{P_0}\right) = \int_{R_{min}}^{R_{max}} N\left(\frac{P}{P_0}, R\right) f(R)\,dR, \quad (8)$$

where $N\left(\frac{P}{P_0}\right)$ is the data of experimental adsorption isotherms; R is pore size; $N\left(\frac{P}{P_0}, R\right)$ is the isotherm of a single pore with the pore size of R; and $f(R)$ is PSD function. The porous adsorption isotherm is available for pore structure analysis by multiplying numerous single pore adsorption isotherms via the PSD functions corresponding to the covered pore size range under the Tarazona state equation.[33,34] As one of the most advanced computation models for PSD analysis, DFT has been widely applied to various porous materials, especially nanoporous carbon, with a main measurement range of 0.35-100 nm.[35,36] Normally the computation models based on traditional macroscopic thermodynamics (such as D-R, BJH or H-K) assume gas to be in a macroscopic-free state and neglect the restriction on the molecule motion in micropores or slot-shaped pores, causing the pore size underestimation. On the other hand, DFT can match the molecular properties of gas adsorbate with the adsorption properties in corresponding pore size range.[33] Furthermore, the isotherms can be associated with the microscopic properties of adsorbate-adsorbent systems in DFT calculation to effectively reduce error. Hence, the pore structure is analyzed based on DFT method in this work.

2.2.3 | NMRC experiment

The NMRC experiment is performed through the cycle of freezing and thawing using distilled water as the probe. Samples were first ground into pillars of 1.5 cm in diameter. Thereafter, preparatory work including drying, vacuum pumping, and pressurized water saturation was carried out. The NMRC experiment began on an NMRC12-010V low-temperature spectrum analyzer with a main frequency of 11.053 MHz. Figure 2D illustrates the experimental set-up. Samples were first cooled to -30°C and then gradually heated to 0.2°C through gas injection from the cold trough, with the temperature intervals varying from 0.1 to 2°C. The sample cell was furnished with a magnetic field. After remaining at each temperature point for 10 minutes, the changes in NMR signals from emitted to collected can be recorded by the IPC & radio frequency cabinet. Finally, the pore volume can be reached by determining the volume of melted water under the corresponding pore size. The core principle is to establish a relationship between the transformation temperature of the probe and the corresponding pore size based on the Gibbs-Thomson thermodynamic equation[37]:

$$\Delta T_m = T_m(r) - T_m^{\infty} = -\frac{4\delta_{sl}T_m^{\infty}}{r\Delta H_f \rho_s}, \quad (9)$$

where r is the pore size; $T_m(r)$ is the melting point of crystal with a diameter of r; T_m^{∞} is the melting point of bulk crystal; δ_{sl} is the surface energy of the crystal and liquid interface;

ΔH_f is the melting enthalpy of macroscopic substances; and ρ_s is the solid density.

3 | RESULTS

Based on the IUPAC[31] and Hodot[38] pore classification, the pores can be divided by diameter into supermicropores (<2 nm), micropores (2–10 nm), transition pores (10–100 nm), and mesopores (100–1000 nm).[39] Pore structure parameters obtained from CO_2 adsorption and NMRC, respectively, are shown in Tables 1 and 2.

3.1 | Measurement of supermicropores with CO_2 adsorption

Figure 4A1,B1 display the supermicropore distribution in semianthracite and anthracite, respectively. The PSD exhibits a typical bimodal distribution that is broadly unified among the 12 samples. The pore volume of the first peak (0.50-0.65 nm in pore size) is higher than that of the second (0.85-0.90 nm in pore size). Moreover, for the first peak anthracite shows a larger pore volume than semianthracite, while for the second peak there is little difference. Comparing the CO_2 adsorption curves (Figure 4A2,B2), the gas adsorption capacity of anthracite is obviously higher than that of semianthracite.

3.2 | Measurement of micropores, transition pores, and mesopores with NMRC

The PSD of semianthracite and anthracite measured by NMRC with diameters ranging from 1 to 500 nm can be divided into two types. As shown in Figure 5, type I displays a relatively uniform distribution of among micropores, transition pores, and mesopores. The jagged curve has multiple

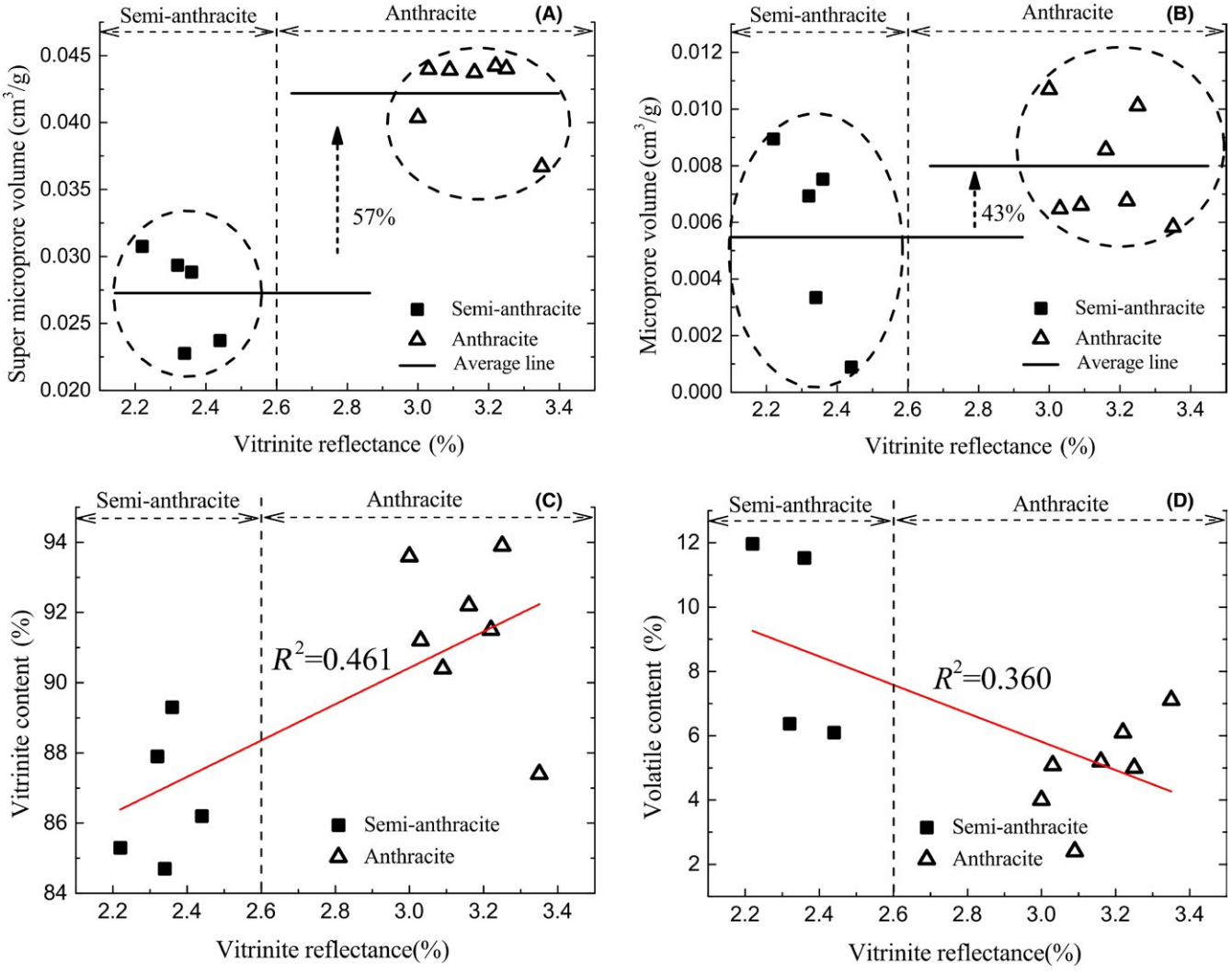

FIGURE 8 Changes in parameters from semianthracite to anthracite. A, Supermicropore volume. B, Micropore volume. C, Vitrinite content. D, Volatile content

peaks and the pore volume between adjacent pore sizes varies greatly and frequently, revealing high complexity and heterogeneity of the pore structure. The PSD of type II presents a decreased pore volume with pore size. The pore volumes that ranged from large to small is in the order of micropores, transition pores, and mesopores.

3.3 | Observation and statistics with FESEM

Through precise imaging under FESEM, multiple pores can be divided into two types: OM-hosted and mineral-associated pores. OM-hosted pores occur as round, elliptical or water drop-shaped stomata with smooth edges and few minerals filled inside (Figure 6A). Single OM pores are generally small, with diameters less than 400 nm. Most of these are scattered with poor connectivity. Mineral-associated pores are defined as the pores associated with minerals (both crystalline minerals and amorphous inorganic components), including corrosion pores, mold pores, intercrystalline pores, etc.[40–42] In high-rank coals, mineral pores are quite irregular both in size and morphology, and generally show angular edges due to deformation force (Figure 6B). The direction of the elongated pores is primarily consistent with the overall orientation of the mineral grains.

The areal porosity calculated by formulas (1)-(5) is approximately 0.44%, in which the pores with diameters <500 nm account for 86% (Table 3). The lower porosity may be because the original surface roughness cannot be displayed under FESEM. Additionally, the sharper and protruding morphology at the edge of pores may also cause an underestimate. For total coal composition, OM and minerals account for 91.91% and 8.09%, respectively, whereas OM pores and mineral pores contribute 25.49% and 74.51% to the total pores, respectively. The reason is that besides the effect of compaction and cementation, a large amount of secondary OM produced during long-term coalification for high- rank coals preferentially fills OM pores,[43] leading to less development in the matrix.

4 | DISCUSSION

4.1 | Coalification jump from semianthracite to anthracite

Figure 1 illustrates the location and tectonic environment of sampling points. Yangquan and Shouyang blocks are located in the northeastern margin of the Qinshui Basin. As affected by magmatic intrusion from the northeast,[44] the coal rank in the study area is gradually changing from anthracite to semianthracite. As shown in Figure 7A, the blocks are close to the magmatic belt of the Yanshanian stage with concealed intrusive body at the bottom, which could cause anomalous thermality in the deep. Based on the high-temperature roasting effect of magma, the coals experience the regional magmatic thermal metamorphism besides initial plutonic metamorphism, which causes a coalification jump from semianthracite to anthracite.[45] During the process, a

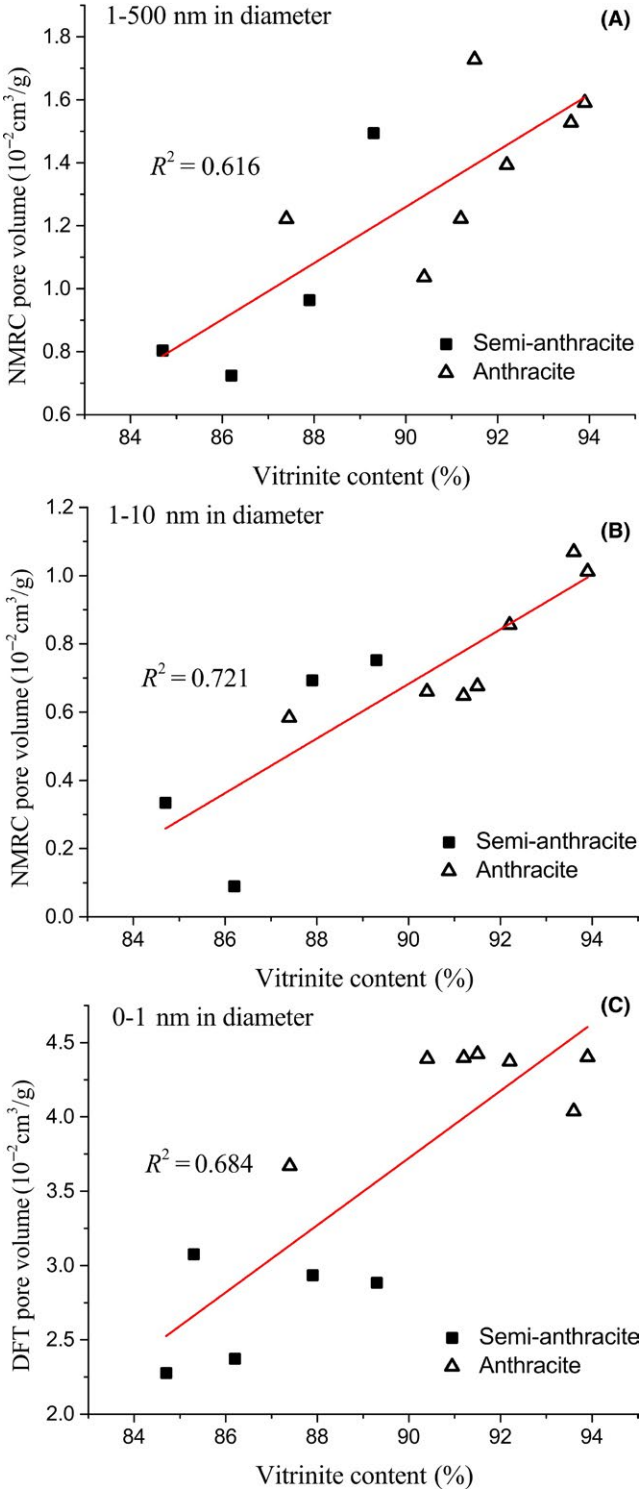

FIGURE 9 The relationship between cumulative volume and vitrinite content. A, 1-500 nm in diameter. B, 2-10 nm in diameter. C, 0-1 nm in diameter

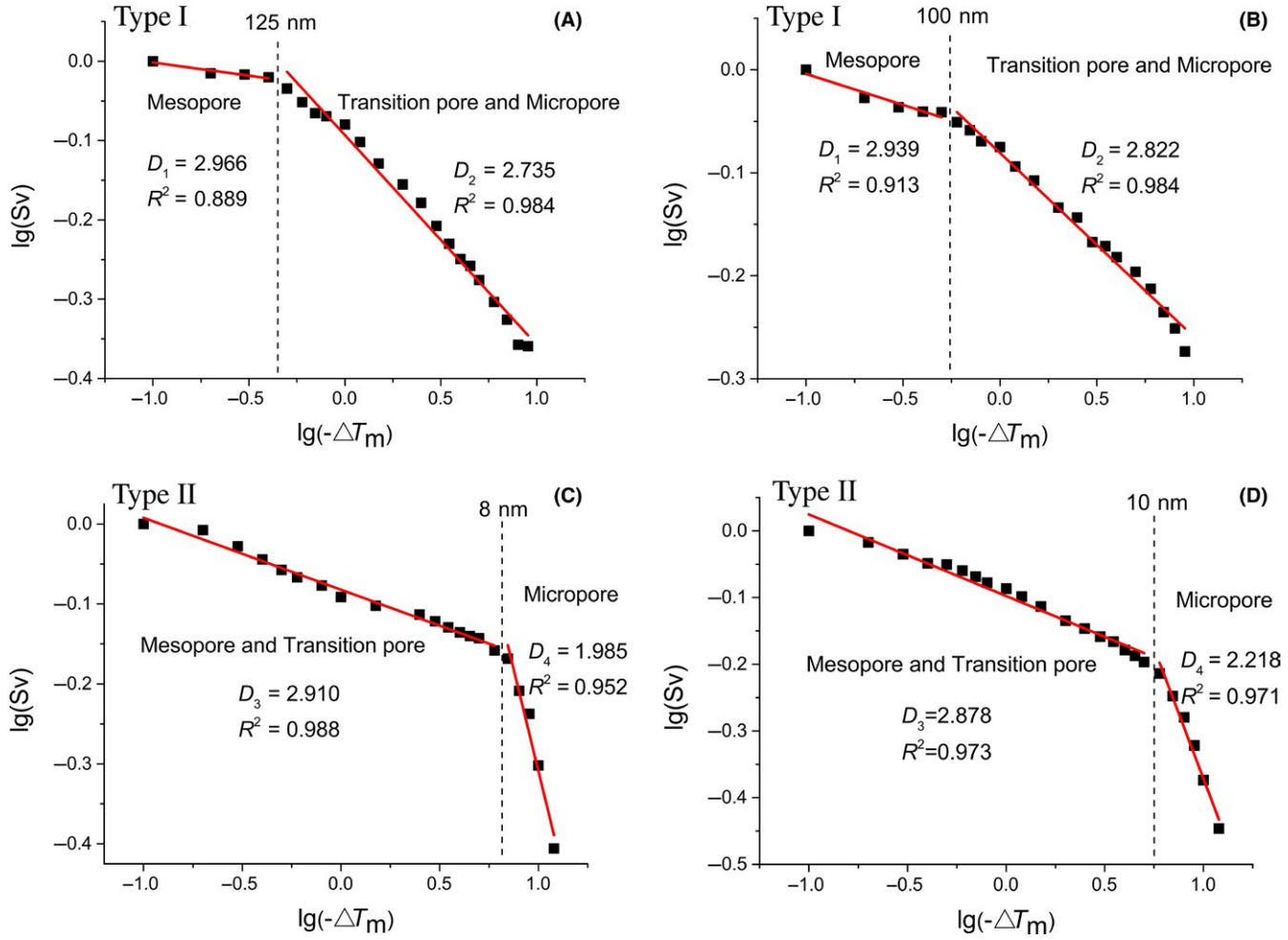

FIGURE 10 Plots of lg(Sv) vs. lg($-\Delta T_m$) for NMRC fractal calculation. A and B, respect S10 and S11 samples of type I pore structure. C and D, respect S3, S7 samples of type II pore structure

TABLE 4 Fractal dimensions based on NMRC analyses and the correlation coefficient

	Type I Samples							Type II Samples					
Sample no.	D_1	R_1^2	D_2	R_2^2	D	R^2	Sample no.	D_3	R_3^2	D_4	R_4^2	D	R^2
S2	2.998	0.905	2.587	0.931	2.686	0.867	S3	2.91	0.988	1.985	0.952	2.866	0.726
S4	2.955	0.632	2.656	0.933	2.742	0.877	S6	2.849	0.881	1.686	0.982	2.608	0.744
S5	2.964	0.912	2.621	0.898	2.724	0.839	S7	2.878	0.973	2.218	0.97	2.82	0.83
S10	2.966	0.889	2.735	0.984	2.79	0.925	S8	2.926	0.859	2.441	0.989	2.808	0.778
S11	2.939	0.912	2.822	0.984	2.858	0.945	S9	2.943	0.963	2.644	0.918	2.85	0.801

D_1, D_2, D_3, D_4 and D respect the fractal dimensions of mesopores, transition pores and micropores for type I pore structure and mesopores and transition pores, micropores for type II pore structure and total pores, respectively. R_1^2, R_2^2, R_3^2, R_4^2 and R^2 respect the correlation coefficients corresponding to D_1, D_2, D_3, D_4 and D, respectively.

large amount of volatile matter in coal seems to get lost. As shown in Figure 8D, there is a negative correlation between the volatile content and vitrinite reflectance. Generally, the influence of magma is directly related to the distance of coals from the intrusive body. The shorter the distance is, the stronger the metamorphism will be (Figure 1). However, the S5 sample is located far from the intrusion while its vitrinite reflectance is rather high. This phenomenon is attributed to the coals that are situated in the steep-slope belt with a large paleoburial depth.[44,46] The coal evolution is dominated by plutonic metamorphism.

Under the thermal metamorphism, coals generate hydrocarbons rapidly, accompanied by creating a large number of stomas with a small aperture. Taking $R_{o,m}$

approximately 2.6% as the boundary, a clear jump in pore volume indicates a large formation of supermicropores and micropores during the coalification from semianthracite to anthracite(Figure 8A,B). In addition, minerals gradually infiltrate into the coal reservoir through groundwater flow, resulting in primary pore partially getting filled. As shown in Figure 7B, the volume of supermicropores and micropores increased by 57% and 43%, respectively, while the volume of the transition pore and mesopore decreased slightly, by 17% and 23%, respectively.

As shown in Figure 8C, vitrinite get purified and enriched in the process of the rapid maturation of coal reservoir, with the increased content by about 10%. The inertinite proportion gets reduced accordingly. Vitrinite possesses strong thermoplasticity and high methane-generating capacity compared to other components,[47] which is beneficial for the development of the microporous structure. As shown in Figure 9, the pore volume (<500 nm in diameter) increases continuously with vitrinite content, especially for micropore and supermicropore. In the semianthracite sample which is less affected by the magma baking, stomas mostly occur sporadically (Figure 6C). While for the anthracite, stomas are more concentrated and often associated with other types of pores, like corrosion pores in Figure 6F. As shown in Figure 6D, a stomatal group appears in homocollinite, with smooth edges, clear outlines, and few minerals filled in. Moreover, the stomas are prone to get deformed during thermal expansion and contraction. It can be found that the deformation of pores with a large diameter is more obvious for the poor stress-bearing capacity and high temperature sensitivity (Figure 6D,G). By comparison, the pores with small diameter can retain better circular or elliptical shape, and the long axes are mostly oriented (Figure 6E,F).

4.2 | Fractal characterizations from micropores to mesopores of anthracite

The fractal theory has been widely applied to quantitatively study the irregular structure of porous material, which has a certain degree of self-similarity.[48,49] The analysis via CO_2 adsorption is meaningless due to the narrow range of radius. In this paper, the fractal characteristics were investigated based on NMRC to discuss the heterogeneity of pore structure. Corresponding to the Gibbs-Thomson thermodynamic equation (Equation 9), fractal dimensions can be obtained to determine the pore volume complexity in NMRC.[22,37,50]

$$\mathrm{Sv}=\left(\frac{r}{r_{\max}}\right)^{3-D}=\left(\frac{\Delta T_{\mathrm{m}}\max}{\Delta T_{\mathrm{m}}}\right)^{3-D} \tag{10}$$

$$\lg(\mathrm{Sv})=(D-3)\lg\left(-\Delta T_{\mathrm{m}}\right)+(3-\mathrm{D})\lg\left(-\Delta T_{\mathrm{m\,max}}\right), \tag{11}$$

where $r_{\max}$ is the maximum of pore diameter, Sv is the percentage of accumulating volume in the total pore volume when pore size is less than r. The fractal dimension D can be calculated by the slope in the linear plot of lg(Sv) against lg $(-\Delta T_{\mathrm{m}})$.

As shown in Figure 10, the aperture fractal dimensions from the NMRC experiment are applied. Pores can be divided into multiple segments of fractal geometry bodies according to the turning point of the slope. The two kinds of pore structure divided in section 3.2 exhibit different fractal features (shown in Figure 10A–B and C–D, respectively). The

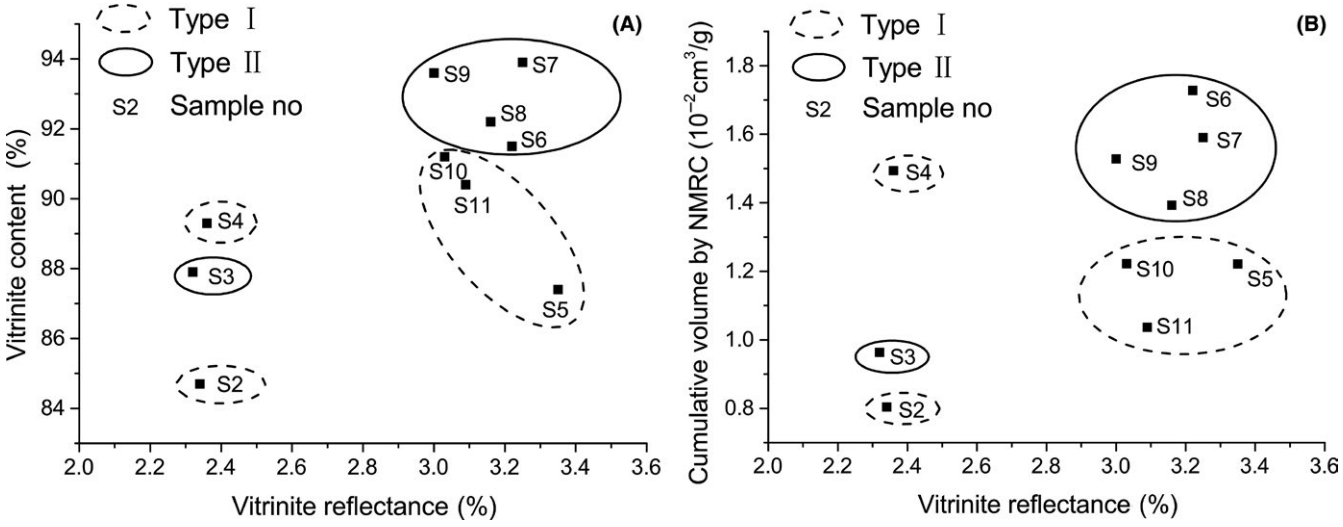

FIGURE 11 Comparison of sample properties between coals with PSD of type I and type II. A, Vitrinite content. B, Cumulative volume by NMRC

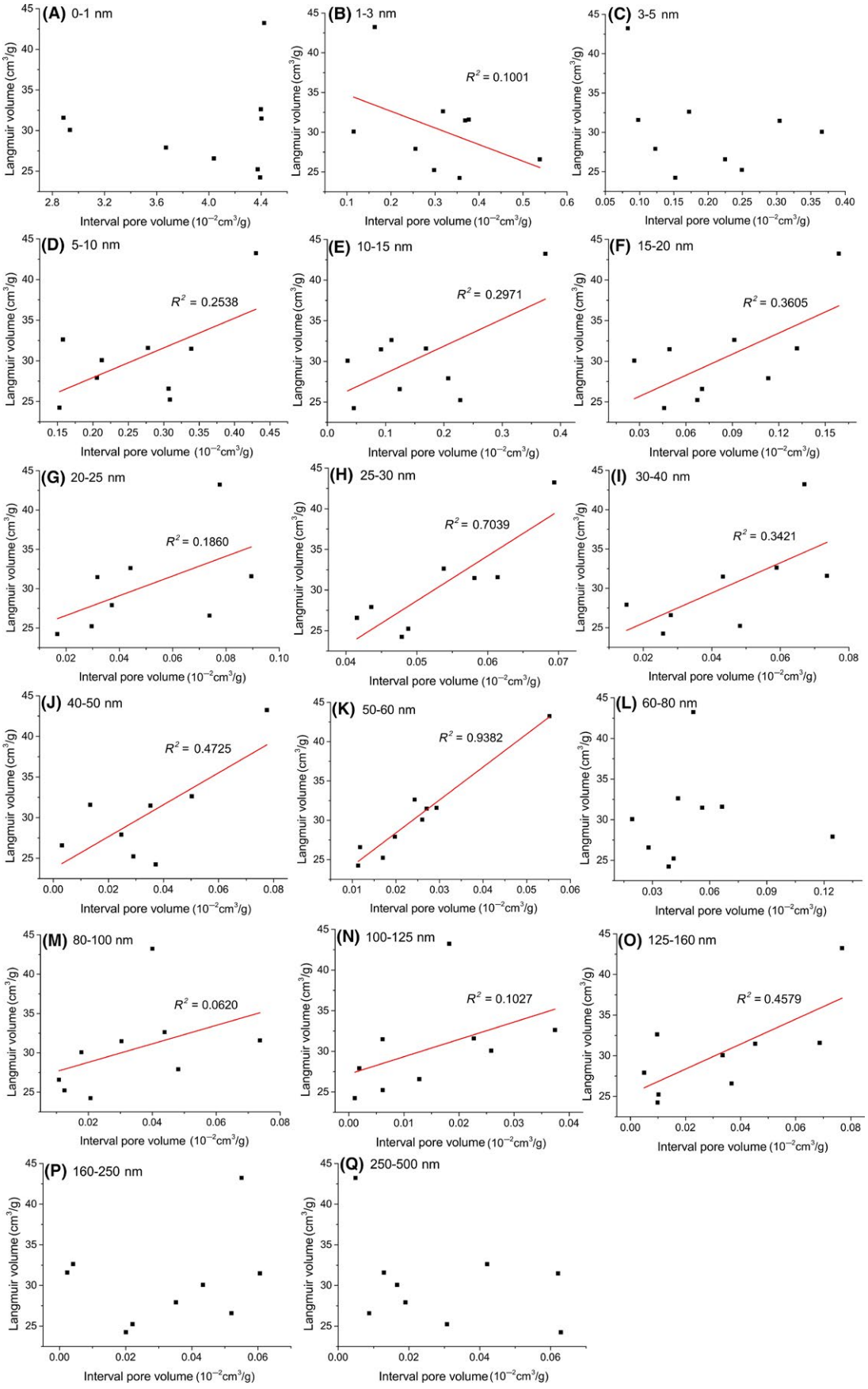

FIGURE 12 The linear fitting of V_L and the pore volume at different size sections

turning points of type I are mainly distributed in the range of 100-125 nm, displaying a high similarity of heterogeneity between transition pores and micropores. In addition, mesopores obviously show a higher complexity than transition pores and micropores. While for the type II pore structure, the turning points appear from 8 to 20 nm and the micropores turn to show a much smaller degree of heterogeneity than transition pores and mesopores. The R^2 in every segment is basically higher than 0.85, with an average value of 0.923(data are shown in Table 4), which indicates that each of the segment can be regarded as an integral fractal system.

The average values of type I fractal dimensions of mesopores (D_1), transition pores and micropores(D_2), and type II fractal dimensions of mesopores and transitions(D_3) and micropores(D_4) are 2.964, 2.684, 2.901, and 2.195, respectively, that is, $D_1>D_3>D_2>D_4$. The results represent that the heterogeneity is increasing with the decrease in pore size. Moreover, the pore structure of type I is more complex than that of type II. The different properties between the type I and type II pore structure could be influenced by the vitrinite content. As shown in Figure 11, the vitrinite content and cumulative volume of type II are both higher than that of type I for anthracites; the phenomenon is not obvious for semianthracites. Vitrinite originating from the lignin and cellulose of xylem and parenchyma of plant stems, leaves and roots is normally characterized by a high degree of homogenization and brittleness. Pores and fractures are more inclined to be developed in vitrinite. A higher content of vitrinite is beneficial to the increase in pore volume, especially for micropores. As a result, the type II samples display a significantly larger pore volume, especially micropores than type I in the PSD curves. Moreover, OM especially vitrinite produces a large number of micropores in coalification, which is a process of order improvement. With the increase in pore volume, the porous throat structure gradually reduces the roughness and improves connectivity.

4.3 | Relationship between pore structure and adsorption capacity

4.3.1 | Influence of pore size distribution on adsorption capacity

Figures 12 and 13 show the relationship between V_L and the pore volume at different size groups. The correlation

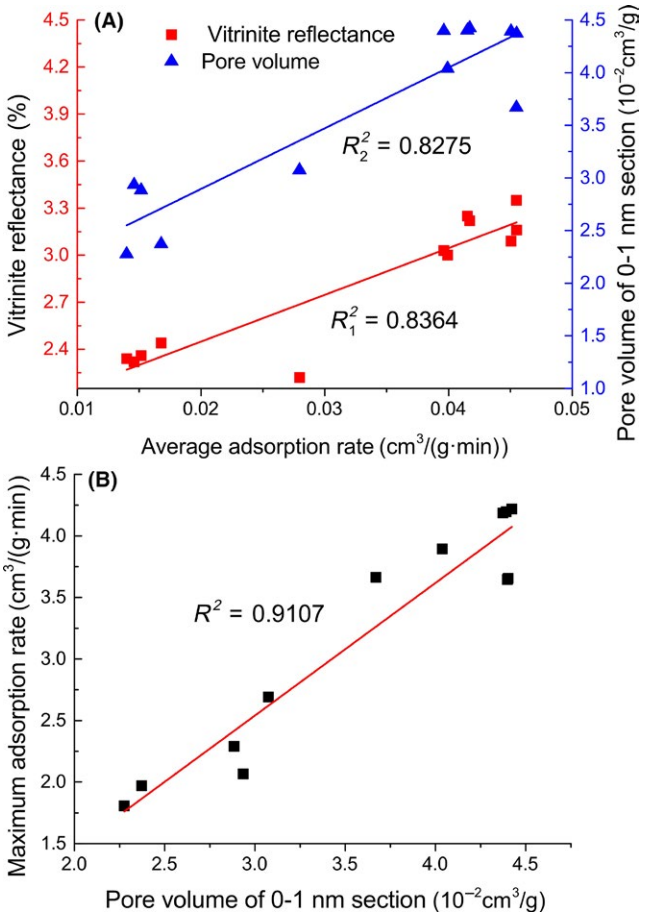

FIGURE 14 The correlation between $R_{o,m}$, pore volume and the adsorption rate of CO_2. A, Average adsorption rate. B, Maximum adsorption rate

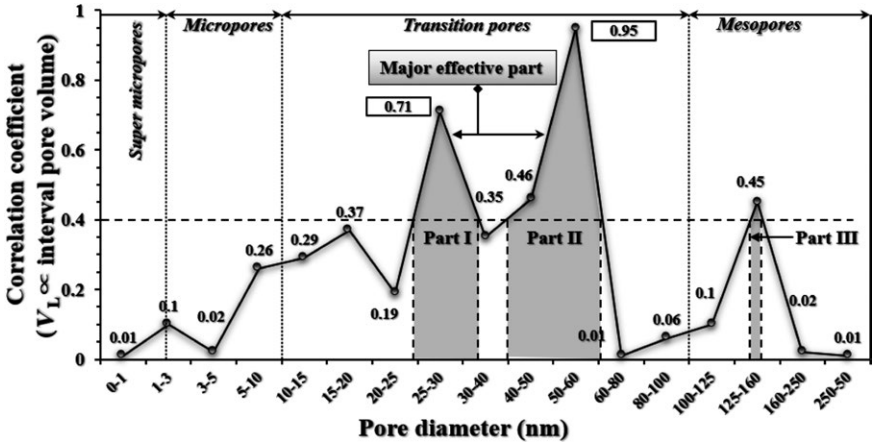

FIGURE 13 The correlation coefficients of Figure 15 corresponding to different pore size sections

coefficients of transition pores are generally higher than others. Taking R^2 of 0.4 as a boundary, three parts owning high relevance are collected, including 25-30 nm, 40-80 nm, and 125-160 nm in diameter. The reasons for the results are that transition pores are proved to be of relatively high volume and low complexity. Moreover, the OM transition pores are less affected by minerals because of their small diameter.

Supermicropore volume measured by CO_2 adsorption shows no relationship with V_L. The reasons are as follows: first the diameter of the CO_2 molecule is smaller than that of CH_4. The PSD obtained by CO_2 adsorption is below 1 nm, which can only accommodate two CH_4 molecules at the most. Second, the CO_2 molecule has a higher boiling point and deeper adsorption potential [51,52]; therefore, the pores detected by CO_2 may be inaccessible to CBM adsorption. Figure 14A shows a positive correlation between $R_{o,m}$, supermicropore volume and average adsorption rate of CO_2, respectively, with R^2 both above 0.8. The R^2 for maximum adsorption rate even reaches 0.9107 (Figure 14B). Therefore, although the impact on CBM adsorbing or reserving is rather weak, the increase in supermicropore volume with $R_{o,m}$ can effectively improve the adsorption rate and capacity of CO_2.

Figure 13 shows no or weak correlation between V_L and the pore volume with diameters from 1 to 5 nm, which is related to poor connectivity. The reason for the groups of 80-125 nm and above 160 nm might be that the specific surface area increases slowly with pore volume.

4.3.2 | Influence of pore heterogeneity on adsorption capacity

The fractal dimensions acquired by the NMRC experiment can reflect the heterogeneity in coals. Figure 15 shows that the Langmuir volume decreases with increasing the fractal

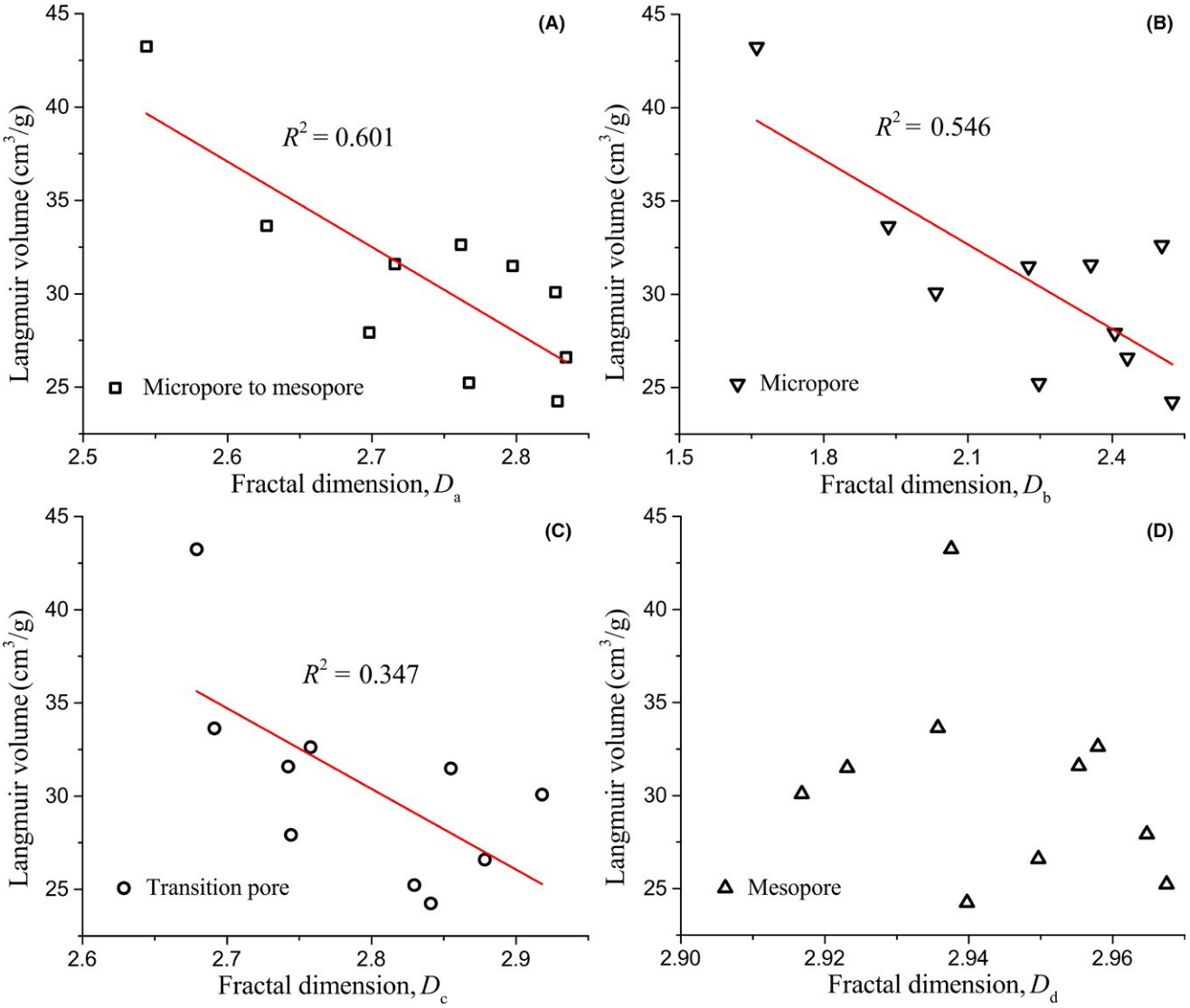

FIGURE 15 The relationship between Langmuir volume and fractal dimension. A, The fractal dimension of micropores, transition pores and mesopores. B, The fractal dimension of micropores. C, The fractal dimension of transition pores. D, The fractal dimension of mesopores

dimensions of the micropore to the mesopore system (1-500 nm in diameter), with a correlation coefficient of 0.601. Moreover, through the fitting of different pore size segments, there is an obvious negative relationship between Langmuir volume and the fractal dimensions of micropore and transition pore, with correlation coefficients of 0.546 and 0.347, respectively. It indicates that increase in pore heterogeneity could reduce the adsorption capacity, in which the complexity of micropore and transition pore is highly influential.

5 | CONCLUSIONS

This research used a combination of FESEM, CO_2 adsorption, and NMRC techniques to systematically study the nanoscale pore structure for high-rank coals with well-developed adsorption pores, to evaluate its impact on adsorption, with the following conclusions:

1. A coalification jump from semianthracite to anthracite occurred in coals of Yangquan and Shouyang blocks due to the magmatic intrusion from the northeast. A large number of stomatal groups were produced based on the high-temperature roasting effect of magma. Changes in parameters including cumulative pore volume, volatile, and vitrinite content occurred during the coalification jump.
2. The pore structure of anthracite in Yangquan and Shouyang blocks acquired from NMRC experiment can be divided into two types according to the pore size distribution and heterogeneity. For type I pore structure, mesopores obviously show higher complexity than transition pores and micropores and there is a high similarity of heterogeneity between transition pores and micropores. While for type II, the micropores turn to show a much smaller degree of heterogeneity than transition pores and mesopores. In addition, the results show that the type II samples display larger pore volume than type I and the pore structure of type I is more complex than that of type II, which is the effect of the vitrinite content.
3. Through fitting V_L and the pore volume at different size groups, transition pores basically show higher correlation coefficients than others, in which the pore volume with diameters of 25-30 nm and 50-60 nm plays a dominant role in CBM adsorption. The supermicropores detected by CO_2 may be inaccessible to CBM adsorption. Moreover, the results show that increase in pore heterogeneity corresponds to lower adsorption capacity, in which the complexity of micropore and transition pore is highly influential.

ACKNOWLEDGEMENTS

This research was funded by the National Natural Science Fund (grant nos. 41830427, 41772160 and 41602170), the National Major Research Program for Science and Technology of China (grant no. 2016ZX05043-001), Key Research and Development Projects of The Xinjiang Uygur Autonomous Region (grant no. 2017B03019-01) and the Fundamental Research Funds for Central Universities (grant no. 2652018002).

ORCID

Yidong Cai https://orcid.org/0000-0002-4915-5615

REFERENCES

1. Gensterblum Y, Ghanizadeh A, Krooss BM. Gas permeability measurements on Australian subbituminous coals: fluid dynamic and poroelastic aspects. *J Nat Gas Sci Eng*. 2014;19:202-214.
2. Zhao JL, Tang DZ, Xu H, Lv YM, Tao S. High production indexes and the key factors in coalbed methane production: a case in the Hancheng block, southeastern Ordos Basin, China. *J Pet Sci Eng*. 2015;130:55-67.
3. Connell L, Mazumder S, Sander R, Camilleri M, Pan Z, Heryanto D. Laboratory characterisation of coal matrix shrinkage, cleat compressibility and the geomechanical properties determining reservoir permeability. *Fuel*. 2016;165:499-512.
4. Tang ZQ, Yang SQ, Zhai C, Xu Q. Coal pores and fracture development during CBM drainage: their promoting effects on the propensity for coal and gas outbursts. *J Nat Gas Sci Eng*. 2018;51:9-17.
5. Pillalamarry M, Harpalani S, Liu SM. Gas diffusion behavior of coal and its impact on production from coalbed methane reservoirs. *Int J Coal Geol*. 2011;86:342-348.
6. Chalmers GR, Bustin RM, Power IM. Characterization of gas shale pore systems by porosimetry, pycnometry, surface area, and field emission scanning electron microscopy/transmission electron microscopy image analyses: examples from the Barnett, Woodford, Haynesville, Marcellus, and Doig unit. *AAPG Bull*. 2012;96:1099-1119.
7. Giffin S, Littke R, Klaver J, Urai JL. Application of BIB–SEM technology to characterize macropore morphology in coal. *Int J Coal Geol*. 2013;114:85-95.
8. Kus J. Application of confocal laser-scanning microscopy (CLSM) to autofluorescent organic and mineral matter in peat, coals and siliciclastic sedimentary rocks — a qualitative approach. *Int J Coal Geol*. 2015;137:1-18.
9. Gaboreau S, Robinet JC, Prêt D. Optimization of pore-network characterization of a compacted clay material by TEM and FIB/SEM imaging. *Micropor Mesopor Mater*. 2016;224:116-128.
10. Gastel RV, Hlawacek G, Dutta S, Poelsema B. Backscattered helium spectroscopy in the helium ion microscope: principles, resolution and applications. *Nucl Instrum Methods*. 2015;344:44-49.
11. Golubev YA, Kovaleva OV, Yushkin NP. Observations and morphological analysis of supermolecular structure of natural bitumens by atomic force microscopy. *Fuel*. 2008;87:32-38.
12. Liu SQ, Sang SX, Wang G, Wang T. FIB-SEM and X-ray CT characterization of interconnected pores in high-rank coal formed from regional metamorphism. *J Pet Sci Eng*. 2017;148:21-31.

13. Pommer M, Milliken K. Pore types and pore-size distributions across thermal maturity, Eagle Ford Formation, southern Texas. *AAPG Bull*. 2015;99:1713-1744.
14. Li HQ, Lin T, Shao HP, Wu CY, Guo ZM, Luo J. Characterization of nanometer tungsten powders. *Rare Met*. 2008;27:197-200.
15. Desbois G, Urai JL, Kukla PA, Konstanty J, Baerled C. High-resolution 3D fabric and porosity model in a tight gas sandstone reservoir: a new approach to investigate microstructures from mm- to nm-scale combining argon beam cross-sectioning and SEM imaging. *J Pet Sci Eng*. 2011;78:243-257.
16. Pan JN, Wang K, Hou QL, Niu QH, Wang HC, Ji ZM. Micropores and fractures of coals analysed by field emission scanning electron microscopy and fractal theory. *Fuel*. 2016;164:277-285.
17. Okolo GN, Everson RC, Neomagus HWJP, Roberts MJ, Sakurovs R. Comparing the porosity and surface areas of coal as measured by gas adsorption, mercury intrusion and SAXS techniques. *Fuel*. 2015;141:293-304.
18. Ravikovitch PI, Bogan BW, Neimark AV. Nitrogen and carbon dioxide adsorption by soils. *Environ Sci Technol*. 2005;39:4990-4995.
19. Cai YD, Liu DM, Pan ZJ, Yao YB, Li JQ, Qiu YK. Pore structure and its impact on CH4 adsorption capacity and flow capability of bituminous and subbituminous coals from Northeast China. *Fuel*. 2013;103:258-268.
20. Tricker MJ, Grint A, Audley GJ, Church SM, Rainey VS, Wright CJ. Application of small-angle neutron scattering (SANS) to the study of coal porosity. *Fuel*. 1983;62:1092-1096.
21. Zhao YX, Sun YF, Liu SM, Wang K, Jiang YD. Pore structure characterization of coal by NMR cryoporometry. *Fuel*. 2017;190:359-369.
22. Yin TT, Liu DM, Cai YD, Zhou YF, Yao YB. Size distribution and fractal characteristics of coal pores through nuclear magnetic resonance cryoporometry. *Energy Fuels*. 2017;31:7746-7757.
23. Cai YD, Li Q, Liu DM, Zhou YF, Lv DW. Insights into matrix compressibility of coals by mercury intrusion porosimetry and N2 adsorption. *Int J Coal Geol*. 2018;200:199-212.
24. Yao YB, Liu DM. Comparison of low-field NMR and mercury intrusion porosimetry in characterizing pore size distributions of coals. *Fuel*. 2012;95:152-158.
25. Yao YB, Liu DM, Xie SB. Quantitative characterization of methane adsorption on coal using a low-field NMR relaxation method. *Int J Coal Geol*. 2014;131:32-40.
26. Radlinski AP, Mastalerz M, Hinde AL, et al. Application of SAXS and SANS in evaluation of porosity, pore size distribution and surface area of coal. *Int J Coal Geol*. 2004;59:245-271.
27. Medek J, Weishauptová Z, Kovář L. Combined isotherm of adsorption and absorption on coal and differentiation of both processes. *Micropor Mesopor Mater*. 2006;89:276-283.
28. Hu GZ, Xu JL, Zhang FX, Zhao CC, Qin W, Zhu YR. Coal and Coalbed methane co-extraction technology based on the ground movement in the Yangquan coalfield, China. *Energies*. 2015;8:6881-6897.
29. Zhou SW, Yan G, Xue HQ, Guo W, Li XB. 2D and 3D nanopore characterization of gas shale in Longmaxi formation based on FIB-SEM. *Mar Pet Geol*. 2016;73:174-180.
30. Cardott BJ, Curtis ME. Identification and nanoporosity of macerals in coal by scanning electron microscopy. *Int J Coal Geol*. 2017;190:205-217.
31. Zhao JL, Xu H, Tang DZ, Mathews JP, Li S, Tao S. A comparative evaluation of coal specific surface area by CO2, and N2, adsorption and its influence on CH4, adsorption capacity at different pore sizes. *Fuel*. 2016;183:420-431.
32. Blacher S, Sahouli B, Heinrichs B, Lodewyckx P, Pirard R, Pirard JP. Micropore size distributions of activated carbons. *Langmuir*. 2000;16:6754-6756.
33. Olivier JP. Modeling physical adsorption on porous and nonporous solids using density functional theory. *J Porous Mater*. 1995;2:9-17.
34. Kowalczyk P, Gauden PA, Furmaniak S, et al. Morphologically disordered pore model for characterization of micro-mesoporous carbons. *Carbon*. 2016;111:358-370.
35. Song Y, Jiang B, Li FL, Liu GJ. Structure and fractal characteristic of micro- and meso-pores in low, middle-rank tectonic deformed coals by CO_2 and N_2 adsorption. *Micropor Mesopor Mater*. 2017;253:191-202.
36. Souza TNVD, Carvalho SMLD, Vieira MGA, Silva MGCD, Brasil DDSB. Adsorption of basic dyes onto activated carbon: experimental and theoretical investigation of chemical reactivity of basic dyes using DFT-based descriptors. *Appl Surf Sci*. 2018;448:662-670.
37. Mitchell J, Webber JBW, Strange JH. Nuclear magnetic resonance cryoporometry. *Phys Rep*. 2008;461:1-36.
38. Hodot BB. *Outburst of Coal and Coalbed Gas (Chinese Translation)*. Beijing, China: China Coal Industry Press; 1966, 318.
39. Zhou SD, Liu DM, Cai YD, Li ZT. 3D characterization and quantitative evaluation of pore-fracture networks of two Chinese coals using FIB-SEM tomography. *Int J Coal Geol*. 2017;174:41-54.
40. Zhao YX, Sun YF, Liu SM, Chen ZW, Yuan L. Pore structure characterization of coal by synchrotron radiation nano-CT. *Fuel*. 2018;215:102-110.
41. Li XC, Kang YL, Haghighi M. Investigation of pore size distributions of coals with different structures by nuclear magnetic resonance (NMR) and mercury intrusion porosimetry (MIP). *Measurement*. 2018;116:122-128.
42. Zhou SD, Liu DM, Cai YD, Yao YB. Gas sorption and flow capabilities of lignite, subbituminous and high-volatile bituminous coals in the Southern Junggar Basin, NW China. *J Nat Gas Sci Eng*. 2016;34:6-21.
43. Li Y, Zhang C, Tang DZ, et al. Coal pore size distributions controlled by the coalification process: an experimental study of coals from the Junggar, Ordos and Qinshui basins in China. *Fuel*. 2017;206:352-363.
44. Yao YB, Liu DM. Effects of igneous intrusions on coal petrology, pore-fracture and coalbed methane characteristics in Hongyang, Handan and Huaibei coalfields, North China. *Int J Coal Geol*. 2012;96–97:72-81.
45. Cai YD, Liu DM, Yao YB, Li JQ, Qiu YK. Geological controls on prediction of coalbed methane of no. 3 coal seam in Southern Qinshui Basin, North China. *Int J Coal Geol*. 2011;88:101-112.
46. Su XB, Lin XY, Zhao MJ, Song Y, Liu SB. The upper Paleozoic coalbed methane system in the Qinshui basin, China. *AAPG Bull*. 2005;89:81-100.
47. Wu JG, Tang DZ, Li S, Wang A, Tang HL. Characteristics of the pore-microfracture system of coal reservoirs in Enhong area, Yunnan province. *Coal Geol Explor*. 2012;40:29-33. (in Chinese with an English abstract).
48. Grau J, Méndez V, Tarquis AM, Díaz MC, Saa A. Comparison of gliding box and box-counting methods in soil image analysis. *Geoderma*. 2006;134:349-359.
49. Shi XH, Pan JN, Hou QL, et al. Micrometer-scale fractures in coal related to coal rank based on micro-CT scanning and fractal theory. *Fuel*. 2018;212:162-172.

50. Petrov OV, Furó I. NMR cryoporometry: principles, applications and potential. *Prog Nucl Magn Reson Spectrosc*. 2009;54:97-122.
51. Crosdale PJ, Beamish BB, Valix M. Coalbed methane sorption related to coal composition. *Int J Coal Geol*. 1998;35:147-158.
52. Bhowmik S, Dutta P. Adsorption rate characteristics of methane and CO_2 in coal samples from Raniganj and Jharia coalfields of India. *Int J Coal Geol*. 2013;113:50-59.

How to cite this article: Yin T, Liu D, Cai Y, Zhou Y. Methane adsorption constrained by pore structure in high-rank coals using FESEM, CO_2 adsorption, and NMRC techniques. *Energy Sci Eng*. 2019;7:255-271. https://doi.org/10.1002/ese3.275